Available online at www.sciencedirect.com
ScienceDirect
Trans. Nonferrous Met. Soc. China 26(2016) 1032−1043
Transactions of Nonferrous Metals Society of China
www.tnmsc.cn

Hot deformation behavior of spray forming LSHR alloy using constitutive equation and processing map

Yi XU, Jie WANG

School of Materials Science and Engineering, Southwest Jiaotong University, Chengdu 610031, China

Received 3 May 2015; accepted 21 August 2015

Abstract: Flow behaviors of spray forming low solvus high refractory (LSHR) alloy were investigated using hot compression tests performed on a Gleeble−3500 thermal mechanical simulator at temperatures of 1020−1150 °C and strain rates of 0.0003−1.0 s^{-1}. The constitutive equation was established, power dissipation (η) maps and hot processing maps were plotted. The microstructure evolution and dislocation distribution of domains with different values of η in power dissipation maps were also observed. The results show that the flow stress increases with decreasing temperature and increasing strain rate. The activation energy of the spray forming LSHR alloy is 1243.86 kJ/mol. When the value of η is 0.36 at the strain of 0.5, the domain in the processing map shows characteristics of typical dynamic recrystallization (DRX) and low dislocation density. According to the microstructure evolution and processing maps, the optimum processing condition for good hot workability of spray forming LSHR alloy can be summed up as: temperature range 1110−1150 °C; strain rate range 0.01−0.3 s^{-1}.

Key words: low solvus high refractory alloy; flow behavior; workability; power dissipation map; processing map; dynamic recrystallization

1 Introduction

Nickel-based superalloys are widely used for turbine disks and blades in aircraft engines and industrial gas turbines due to their excellent mechanical properties at high temperatures [1−3]. As the typical third generation powder metallurgy superalloy, low solvus high refractory (LSHR) alloy possesses high strength at temperatures of 700−760 °C, but insufficient creep resistance at higher temperatures [4].

Based on the published chemical compositions of the typical third generation powder metallurgy (P/M) superalloys [5−7], the LSHR alloy is manufactured by using spray forming process. As potential near-net shape benefits, the primary advantage of the spray forming process is the ability to manufacture alloy compositions that are problematical in conventional processes such as ingot casting, direct chill casting, and powder metallurgy. The main disadvantage of spray forming is as-sprayed porosity [8].

For porosity that affects mechanical properties of the alloy, the need for a subsequent isothermal forging or other downstream processes is well recognized. For spray forming LSHR alloy of this study, controlling the isothermal forging processes to attain a uniform and dense microstructure seems to be very important. Thus, a systematic research of the hot deformation behavior of the alloy is essential. The workability of materials can be described by true stress−true strain curves in some sense [9−12]. In addition, it is governed by the initial microstructure and the externally imposed stress state, both of which vary with deformation process [13−15]. Constitutive equation can be used to describe the change of flow stress with the variation of processing parameters such as deformation strain, temperature and strain rate [16−18]. It is one of the most important inputs for the numerical simulation of isothermal forging [19]. Although the optimum hot deformation processing parameters can be determined by the trial and error methods, the recently developing processing map based on dynamic material model (DMM) is considered a very useful tool for evaluating the hot deformation mechanisms and optimizing deformation in

Foundation item: Project (51301143) supported by the National Natural Science Foundation of China; Project (2014M560727) supported by the National Postdoctoral Foundation of China; Project (2015GZ0228) supported by the Sichuan Province Science−Technology Support Plan, China; Project (2682014CX001) supported by the Science and Technology Innovation Project of SWJTU University, China

Corresponding author: Yi XU; Tel: +86-28-87600782; E-mail: xybwbj@swjtu.cn

DOI: 10.1016/S1003-6326(16)64200-0

superalloys [20−23].

LIU et al [21] established the processing map of Ni−20.0Cr−2.5Ti−1.5Nb−1.0Al alloy and obtained the instability domains of plastic deformation. Three instability domains respectively located at around 940 °C, 1.0 s^{-1} and 1060 °C, 0.001 s^{-1} when the strain range was from 0.05 to 0.40 and 1060 °C, 1.0 s^{-1} when the strain range was from 0.45 to 0.70. PU et al [24] discovered that the strain had no influence on processing map of stainless steel S32654, and predicted an instability domain at temperatures below 1175 °C and strain rates above 0.1 s^{-1}. WANG et al [22] built the processing maps of X-750 superalloy at strains of 0.1, 0.3 and 0.5 respectively, and confirmed that the optimum parameters for hot working of the alloy were deformation temperatures of 1000−1050 °C and strain rates of 0.1−1 s^{-1} at the strain of 0.5. SENTHILKUMAR et al [25] studied the relation between the microstructural behavior of Al-based nanocomposite materials and controlled process parameters by processing map. RAJAMUTHAMILSELVAN and RAMANATHAN [26] verified the stable and unstable regions in the processing map with the microstructural observations of the deformed 7075 Al/20%SiC_p composite samples, and identified stable regions with the dynamic recrystallization characteristics and unstable regions such as debonding of SiC particles, matrix crack, and adiabatic shear band formation. Although some studies have been conducted to investigate the high temperature deformation behaviors of Ni-based superalloys, the constitutive models are still not advanced enough to explain the whole complex dynamic deformation mechanisms and microstructure evolution. Most of the above investigations show that the processing maps include power dissipation and instability maps, and both of them can be established by the data obtained from the hot compression tests of the alloys. The most optimal process parameters for hot deformation can be obtained from the analysis of the processing maps and microstructure observations.

In this work, the hot deformation behaviors of spray forming LSHR alloy under different deformation conditions were studied in order to understand the constitutive relationship of the material. The true stress−true strain data were analyzed. Then, constitutive equation was established, power dissipation (η) maps and processing maps were plotted by mathematical analysis and calculation. The microstructures of stability and instability domains in processing maps were also observed. The effects of processing parameters on flow stress, activation energy, power dissipation maps, instability maps and microstructure evolution were investigated.

2 Experimental

The material used for the hot deformation tests in this work is spray forming LSHR alloy manufactured by IWT in Bremen. The chemical composition (mass fraction) is 12.77% Cr, 21.75% Co, 2.95% Mo, 4.12% W, 3.60% Al, 3.54% Ti, 1.51% Nb, 1.52% Ta, 0.023% C, 0.022% B, 0.03% Zr, and Ni balance. The cylindrical specimens with the diameter of 8 mm and the height of 12 mm were machined from as-sprayed billet for hot compression tests to study flow behavior and optimize isothermal forging parameters. Hot compression tests were conducted using a Gleeble−3500 simulator at temperatures of 1020, 1050, 1080, 1110 and 1150 °C and in the strain rate range of 0.0003−1 s^{-1}. All specimens were heated to the deformation temperature at a heating rate of 10 °C/s and held for 120 s in order to gain the uniform temperature field before the hot compression test. Then, they were deformed to a true strain of 50% and water-cooled to room temperature. According to the flow stress record as a function of strain, the flow stress−strain curves at different deformation temperatures and strain rates were obtained using standard equations. Then, power dissipation (η) maps and processing maps were built based on the selected stresses and strains by using an Origin software. The deformed specimens were sectioned parallel to the compression axis and the cut surfaces were prepared for microstructure observation. The microstructures of as-sprayed and deformed samples were observed using a Leica optical microscope (OM) with the chemical etchant of $CuSO_4$ (10 g) + HCl (50 mL) + H_2O (50 mL) at the etching time of 20−40 s. The γ' precipitates and carbides of as-sprayed samples were observed using a Zeiss ultra 55 scanning electron microscope (SEM), and the samples were prepared by electro polishing with 20% H_2SO_4−CH_3OH and followed by electrolytic etching in a CrO_3−H_3PO_4−H_2SO_4 solution at etching time of 20 s.

3 Results and discussion

3.1 Material characteristics

The typical microstructures of spray forming LSHR alloy are shown in Fig. 1. The microstructure reveals prior particle boundaries (PPBs) and obvious droplet deposition flow lines. The PPB network consists of some large primary γ' precipitates and white carbides. SEM observation of the sample reveals cuboidal γ' precipitates (Fig. 1(c)) in the interior of the grains and large petaloid γ' precipitates (Fig. 1(d)) mainly at the grain boundaries, which indicates that there is a tendency of microsegregation at grain boundaries to some extent.

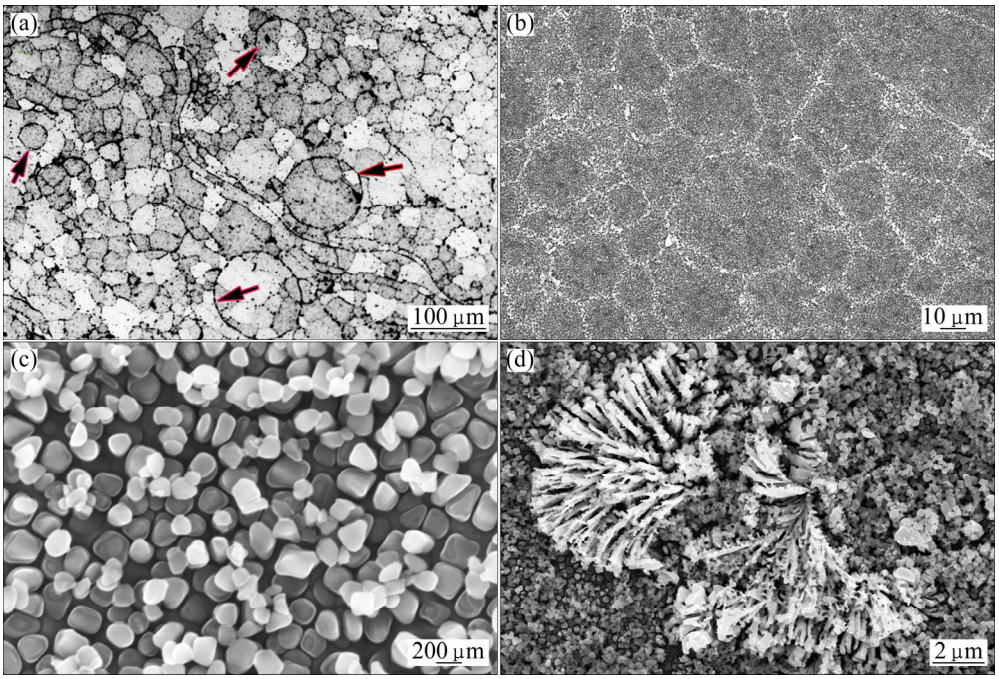

Fig. 1 Microstructures of spray forming LSHR alloy exhibiting some PPBs (marked with arrows) and deposition flow lines (a), carbides at grain boundary (b), cuboidal γ' precipitates in grain (c) and petaloid γ' precipitates at grain boundaries (d)

According to the analysis results of the thermodynamic phase diagram (Fig. 2), the principal phase compositions of spray forming LSHR alloy are γ, γ', MC, $M_{23}C_6$, M_6C and M_3B_2, respectively. The volume fraction of γ' precipitates is 58% and the complete solution temperature is 1205 °C. For increased volume fraction and solution temperature of γ' precipitates, the spray forming LSHR alloy may have a higher deformation resistance at high temperatures during the hot working process.

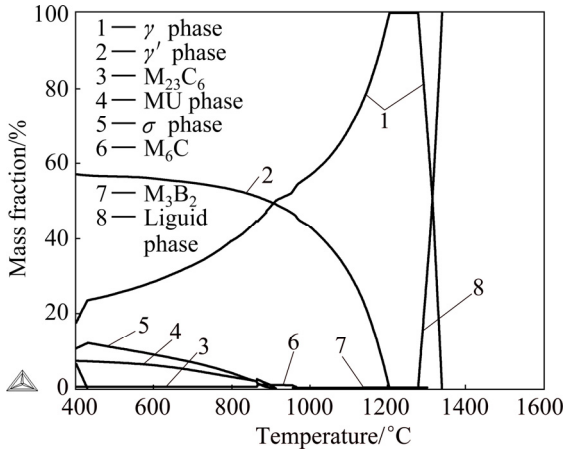

Fig. 2 Thermodynamic phase diagram for spray forming LSHR alloy

3.2 Constitutive equation

The true stress−true strain curves of the spray forming LSHR alloy can be easily transformed from the load−displacement data recorded by Gleeble−3500 simulator during hot compression test. Figure 3 shows the typical true stress−true strain curves obtained from hot compression tests of the alloy. The basic changing trend of flow stress is as follows: the stress increases sharply with increasing strain at first, then decreases when peak stress reaches and is almost stable at different strains finally. The flow curves with a broad peak suggest that the dynamic recrystallization (DRX) is a dominant deformation mechanism. With increasing strain, the stress decreases until a relatively stable stress appears, showing a dynamic flow softening. Some serrations in the flow curves are shown at lower strain rates of 0.0003 and 0.001 s^{-1}, and this result is contrary to the views of others [27]. According to the processing maps and the microstructure observation, it can be confirmed that the serrations in the flow curves at low strain rates are mainly caused by the DRX.

The variation of flow peak stress as a function of deformation temperature and the logarithm of the strain rate can be shown more clearly in Fig. 4. It can be found that the effect of the deformation temperature and strain rate on the flow stress is significant. For the spray forming LSHR alloy, the flow stress decreases with increasing deformation temperature or decreasing strain rate. This is because low strain rates provide sufficient time for energy accumulation, and high temperatures provide higher energy at boundaries for the nucleation and growth of dynamically recrystallized grains and dislocation annihilation, thus resulting in the reduction of

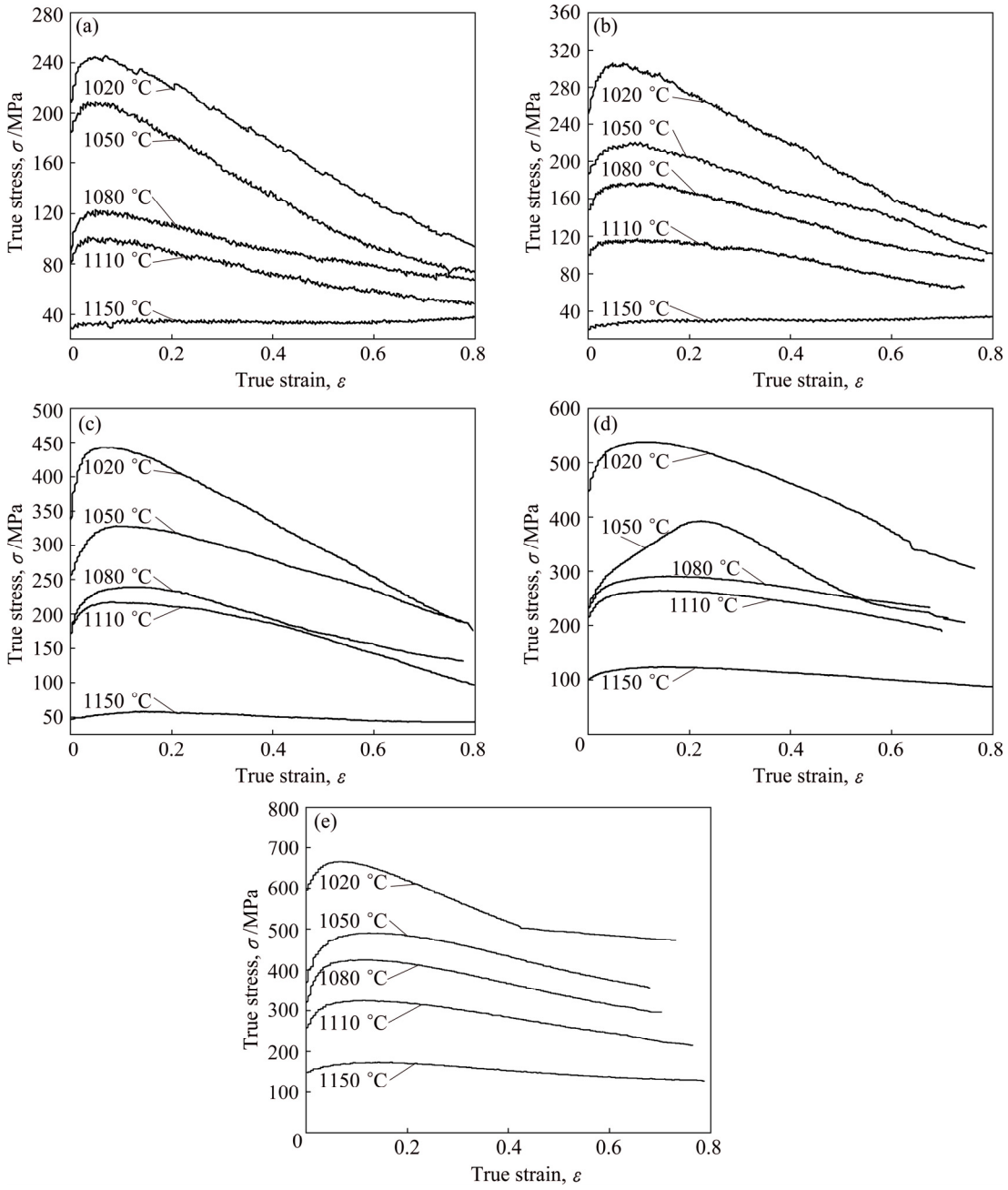

Fig. 3 True stress−true strain flow curves for spray forming LSHR alloy at different temperatures and strain rates: (a) 0.0003 s^{-1}; (b) 0.001 s^{-1}; (c) 0.01 s^{-1}; (d) 0.1 s^{-1}; (e) 1 s^{-1}

the flow stress level. So, the effect of deformation temperature and strain rate on flow stress can be accounted for the terms of DRX and dislocation mechanism.

The stress at high temperatures depends on the deformation temperature (T) and strain rate ($\dot{\varepsilon}$) during the hot deformation process, and the Zener−Hollomon parameter is described as

$$Z = \dot{\varepsilon}\exp\left(\frac{Q}{RT}\right) = f(\sigma) \tag{1}$$

where $\dot{\varepsilon}$ is the strain rate (s^{-1}), Q is the activation energy of deformation (kJ/mol), R is the mole gas constant, T is the deformation temperature (K), and $f(\sigma)$ is the stress function. According to the theoretical analysis, the peak stress, the steady state stress and any variable flow stress should conform to Eq. (1). Generally, the analytic expression equations of stress function $f(\sigma)$ used to describe the plastic deformation of material can be written as follows:

$$f_1(\sigma)=A\sigma^n \tag{2}$$

$$f_2(\sigma)=A\exp(\beta\sigma) \tag{3}$$

$$f_3(\sigma)=A[\sinh(\alpha\sigma)]^n \tag{4}$$

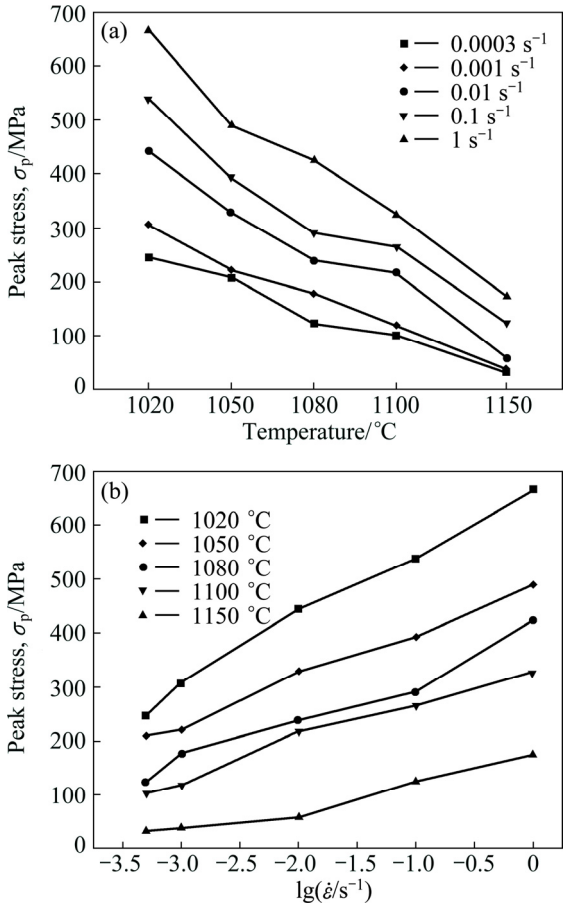

Fig. 4 Effect of processing parameters on peak stress: (a) Deformation temperature; (b) Strain rate

where A (s^{-1}), α (MPa^{-1}) and β (MPa^{-1}) are material constants, m and n are constants related to the strain rate. Based on Eqs. (2) and (3), a hyperbolic sine equation (Eq. (4)) is established that can be used in relatively wide range of stress to accurately describe the deformation behavior of materials. Within the range of deformation conditions used, the peak stress as a function of temperature and strain rate is expressed through combining Eq. (1) with Eq. (4):

$$\dot{\varepsilon} = A[\sinh(\alpha\sigma_{\mathrm{p}})]^n \exp\left(\frac{-Q}{RT}\right) \tag{5}$$

As we know, Eq. (1) can be expressed by a power law (Eq. (2)) when $\alpha\sigma_{\mathrm{p}}<0.8$ and by an exponential law (Eq. (3)) when $\alpha\sigma_{\mathrm{p}}>1.2$. At low stresses, by combining Eq. (1) with Eq. (2), the peak stress can be described by

$$\dot{\varepsilon} = A\sigma_{\mathrm{p}}^{m} \exp\left(\frac{-Q}{RT}\right) \tag{6}$$

At high stresses, combining Eq. (1) with Eq. (3) gives

$$\dot{\varepsilon} = A\exp(\beta\sigma_{\mathrm{p}})\exp\left(\frac{-Q}{RT}\right) \tag{7}$$

So, β and m can be simply determined from experimental data at low and high stresses. Therefore, this study assumes that A, n, α and Q are the material constants that depend on strain. At constant deformation temperatures, the partial differentiation of Eqs. (6) and (7) yields the following equations: $m = \partial\ln\dot{\varepsilon}/\partial\ln\sigma_{\mathrm{p}}$ and $\beta = \partial\ln\dot{\varepsilon}/\partial\ln\sigma_{\mathrm{p}}$. The values of m and β can be given in Fig. 5 from the slope of the lines in the $\ln\sigma_{\mathrm{p}}-\ln\dot{\varepsilon}$ and $\sigma_{\mathrm{p}}-\ln\dot{\varepsilon}$ plots, β=0.02509 MPa^{-1} and m=5.16343. The constants $\alpha=\beta/m$=0.00459 MPa^{-1}.

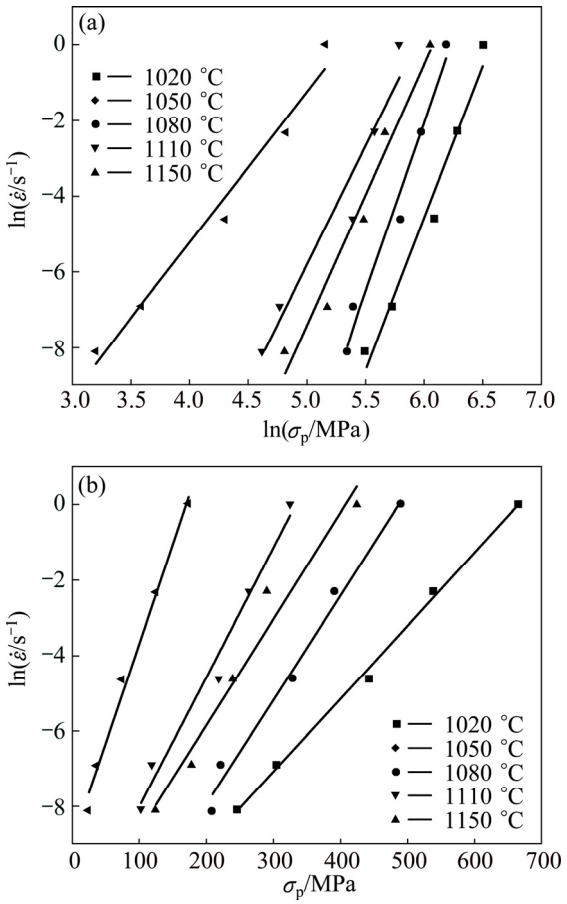

Fig. 5 Relationships between $\ln\dot{\varepsilon}$ and $\ln\sigma_{\mathrm{p}}$ (a), $\ln\dot{\varepsilon}$ and σ_{p} (b) at different temperatures

Taking the natural logarithm of both sides of Eq. (5) gives

$$\ln\dot{\varepsilon} = \ln A + n\ln[\sinh(\alpha\sigma_{\mathrm{p}})]\left(\frac{-Q}{RT}\right) \tag{8}$$

For the given strain rate conditions, differentiating Eq. (9) is rearranged into

$$Q = R\frac{\partial\ln\dot{\varepsilon}}{\partial\ln[\sinh(\alpha\sigma_{\mathrm{p}})]}\bigg|_{T}\frac{\partial[\sinh(\alpha\sigma_{\mathrm{p}})]}{\partial\ln(1/T)}\bigg|_{\dot{\varepsilon}} \tag{9}$$

By substituting the values of flow stress and strain rate for all the tested temperatures into Eq. (8), linear

relationships between $\ln[\sinh(\alpha\sigma_p)]$ and $\ln\dot{\varepsilon}$ and $\ln[\sinh(\alpha\sigma_p)]$ and $1/T$ when T remains constant are shown in Fig. 6. The value of $\left.\frac{\partial \ln\dot{\varepsilon}}{\partial \ln[\sinh(\alpha\sigma_p)]}\right|_T$ can be estimated because n is equal to the linear slope. The average value of $\left.\frac{\partial \ln\dot{\varepsilon}}{\partial \ln[\sinh(\alpha\sigma_p)]}\right|_T$ is 4.522 as determined by calculation. From these similar figures and methods, the average value of $\left.\frac{\partial[\sinh(\alpha\sigma_p)]}{\partial \ln(1/T)}\right|_{\dot{\varepsilon}}$ = 33085 can be easily obtained, and the activation energy Q=1243.86 kJ/mol can be calculated by Eq. (9). The Zener−Hollomon parameter is defined through combining Eq. (1) with Eq. (4):

$$Z=A[\sinh(\alpha\sigma)]^n \tag{10}$$

Taking the natural logarithm of both sides of Eq. (10), we get

$$\ln Z=\ln A+n\ln[\sinh(\alpha\sigma)] \tag{11}$$

A linear relationship of $\ln Z$−$\ln[\sinh(\alpha\sigma)]$ is shown in Fig. 7. The values of n and A are 4.347 and 2.42×10^{45} s^{-1}, respectively. At last, the constitutive equation is formulated as

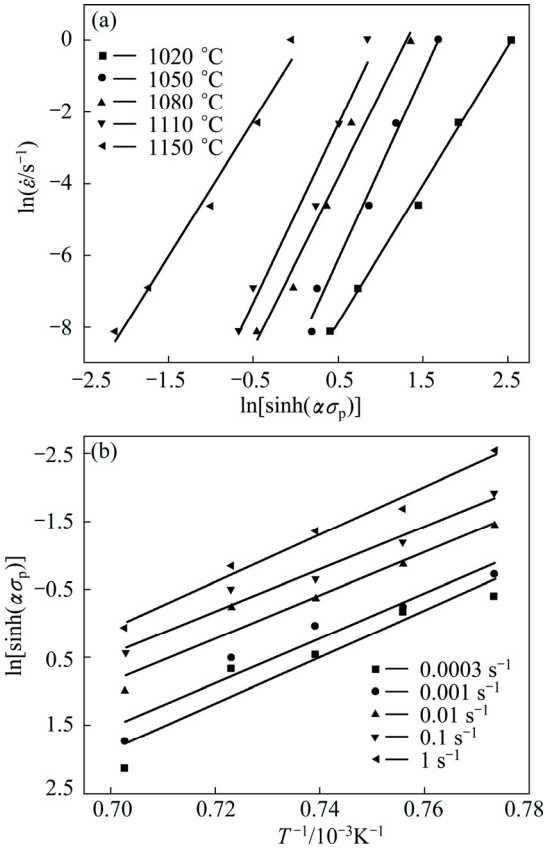

Fig. 6 Relationship between $\ln\dot{\varepsilon}$ and $\ln[\sinh(\alpha\sigma_p)]$ at different temperatures (a), and $\ln[\sinh(\alpha\sigma_p)]$ and $1/T$ at different strain rates (b)

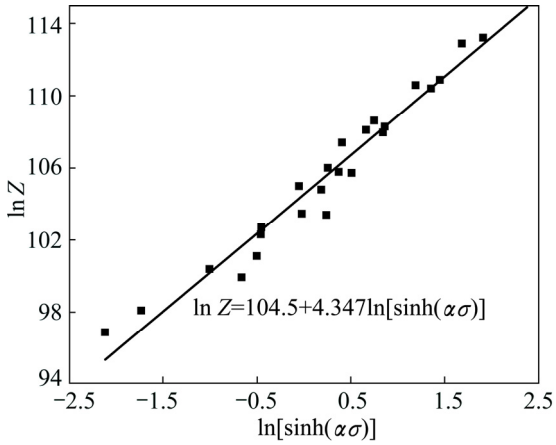

Fig. 7 Plot of Zener−Hollomon parameter as function of flow stress

$$\dot{\varepsilon}=2.42\times10^{45}[\sinh(0.004859\sigma)]^{4.347}\exp\left(-\frac{1243860}{RT}\right) \tag{12}$$

In order to confirm Eq. (12), comparison between the measured and calculated flow stresses of the studied spray forming LSHR alloy was carried out. The correlation coefficients between the experimental data and regression results of peak stress at different temperatures and stress rates are shown in Table 1. The average correlation coefficient is 0.9846, which indicates that the measured value and calculated value of peak stress have a good correlation.

Table 1 Correlation coefficients on measured values and calculated values of peak stress

Stress rate/s^{-1}	Correlation coefficient	Temperature/°C	Correlation coefficient
0.0003	0.9734	1020	0.9954
0.001	0.9811	1050	0.9905
0.01	0.9828	1080	0.9894
0.1	0.9861	1110	0.9699
1	0.9938	1150	0.9836

3.3 Power dissipation map and microstructure evolution

Thermal energy dissipation mainly depends on material flow behavior. The general formula of the flow stress at constant strain and temperature is expressed as

$$\sigma=k\dot{\varepsilon}^r \tag{13}$$

where k is a constant; exponent r, termed as strain rate sensitivity exponent, is given by

$$r=\frac{\partial \ln\sigma}{\partial \ln\dot{\varepsilon}} \tag{14}$$

Based on the dynamic material model (DMM), the

total dissipated power (P) includes two parts of integral that could be calculated according to

$$P=\sigma\dot{\varepsilon}=G+J=\int_0^{\dot{\varepsilon}}\sigma \mathrm{d}\dot{\varepsilon}+\int_0^{\sigma}\dot{\varepsilon}\mathrm{d}\sigma \tag{15}$$

where the first integral is defined as G content which represents the main power input dissipated in the form of a temperature rise. The second integral is defined as J co-content and is related to the power dissipated by microstructure changes including phase transition and DRX. If strain rate has little impact on r in a certain range, ΔJ and ΔG can be given as follows:

$$\Delta J=\int_0^{\sigma+\Delta\sigma}\dot{\varepsilon}\mathrm{d}\sigma \tag{16}$$

$$\Delta G=\int_{\dot{\varepsilon}}^{\dot{\varepsilon}+\Delta\dot{\varepsilon}}\sigma \mathrm{d}\dot{\varepsilon} \tag{17}$$

The efficiency η of power dissipation occurring through microstructure evolution during hot deformation process is deduced by comparing the non-linear power dissipation occurring instantaneously in the deformed samples with the linear power dissipation for which the r value is unity, and is defined as

$$\eta=\frac{\Delta J/\Delta P}{(\Delta J/\Delta P)_{\text{line}}}=\frac{r/(r+1)}{1/2}=\frac{2r}{r+1} \tag{18}$$

The power dissipation map is obtained by plotting iso-efficiency contour map of parameter η. A typical power dissipation map is established in the temperature range of 1050−1150 °C and strain rate range of 0.0003−1 s^{-1} in a strain range of 0.1−0.7 as shown in Fig. 8.

The values of η increase with increasing deformation temperature. Under the deformation conditions of this work, it is also found that the peak zones in the upper corner of η contour maps change from a semi-circle at strains of 0.1, 0.3 and 0.5 into a closed circle at a strain of 0.7. In addition, the peak zones of parameter η always locate in the high temperature range and strain rate range of 0.01−0.3 s^{-1}, except for the contour maps at a strain of 0.7. The values of η gradually increase from 0.38 to 0.50 with increasing strain as a result of the increase of the degree of DRX in the deformed microstructure.

Taking the power dissipation map at a strain of 0.5 as an example, five different domains according to the characteristic values of η are shown in Fig. 8(c). Domain I occurring at 1090−1150 °C and 0.001−0.01 s^{-1} is on the upper left of the map, with η values of 0.18−0.24. Domain II occurring at 1040−1080 °C and 0.001−0.01 s^{-1} locates on the lower left of the map, with η values of 0.30−0.36. Domain III is on the lowest left of

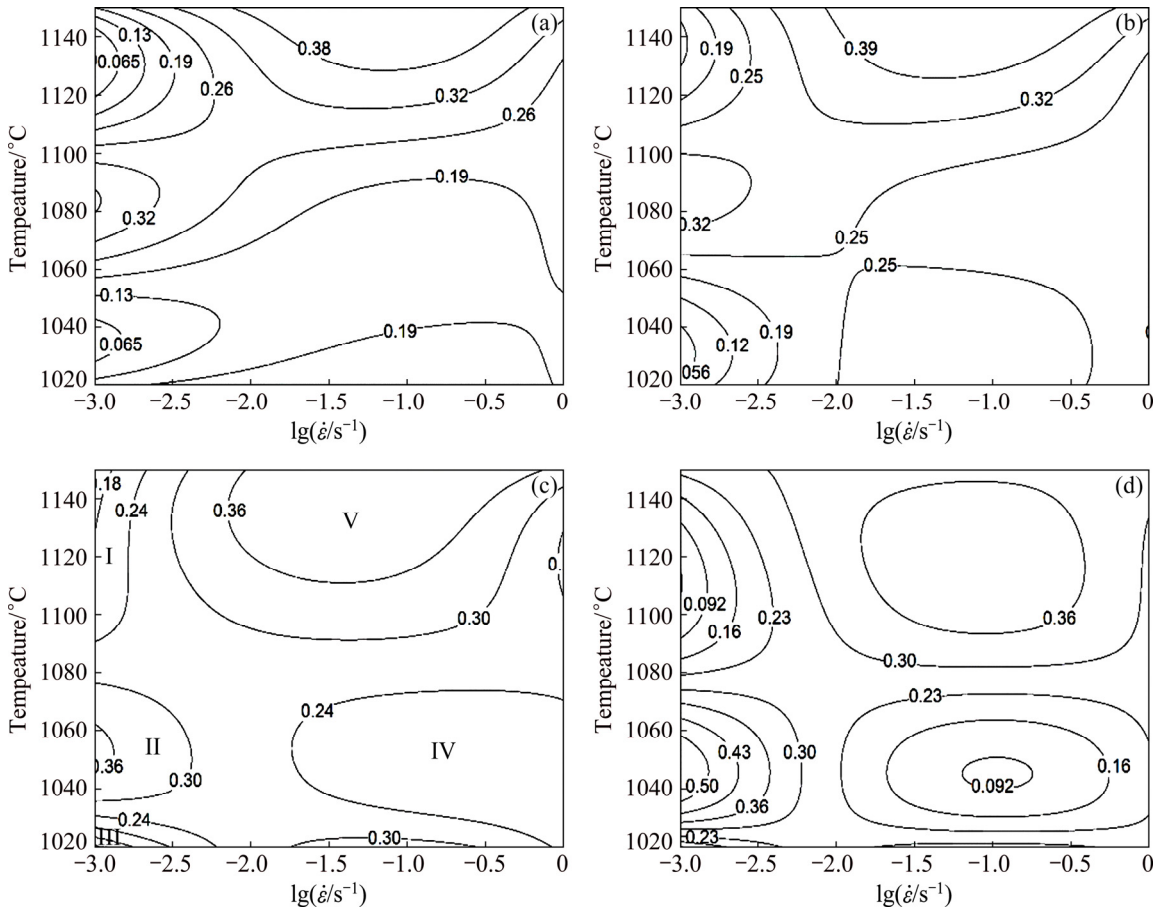

Fig. 8 η contour maps of spray forming LSHR alloy at different strains: (a) ε=0.1; (b) ε=0.3; (c) ε=0.5; (d) ε=0.7

the map and the deformed parameters are temperatures of 1020−1030 °C and strain rates of 0.0003−0.001 s^{-1}, with η values of less than 0.24. Domain IV occurring at 1020−1080 °C and 0.01−1 s^{-1} is on the lower right, with η values of less than 0.24. Domain V occurring at 1110−1150 °C and 0.01−1 s^{-1} is in the middle upper, with η values of more than 0.36. A continuum map can be interpreted in terms of the microstructural processes. The microstructures of spray forming LSHR alloy corresponding to five different domains (Fig. 8(c)) in the power dissipation η map at a strain of 0.5 are shown in Fig. 9. For Domain I, the sample deformed at 1110 °C and 0.01 s^{-1} shows dynamic recrystallization characteristics in the local region (Fig. 9(a)), fine equiaxed recrystallized grains surround long and narrow deformed grains. Typically, the initiation of dynamic recrystallization (DRX) occurs with the growing fluctuations of the grain boundary shape. Serration and bulges then develop, and eventually new grains are generated along the prior grain boundaries [28]. The non-recrystallized grains could be gradually refined after hot deformation due to the occurrence of DRX for many times. For Domains II and III, the samples deformed at 1050 and 1020 °C, and strain rates of 0.001 s^{-1} and 0.0003 s^{-1}, respectively show lots of large deformed non-recrystallized grains, and some ultrafine equiaxed grains surrounding large non-recrystallized grains are called necklace microstructure (Figs. 9(b) and (c)). The necklace is the intermediate microstructure in grain refinement process. When several necklaces are formed, the grains are further refined after hot deformation for the continuous occurrence of DRX. According to the atomistic processing map of RAJ [29], the power dissipation value of dynamic recovery (DRV) is less than that of DRX. For Domain IV with lower values of η, the microstructure of sample at 1050 °C and 0.1 s^{-1} is shown in Fig. 9(d). The deformed grains extend along the direction of deformation, revealing obvious DRV characters. Compared with the above deformed microstructures, the microstructure of Domain V at 1150 °C and 0.01 s^{-1} exhibits the finest and homogeneous equiaxed DRX grains in Fig. 9(e). DRX is considered as a preferential chosen domain for hot workability optimization and good mechanical properties control. Based on the largest values of power dissipation and DRX microstructure characters, Domain V is considered as the domain where the material shows good workability.

Figure 10 shows the dislocation evolution of the deformed samples after hot compression tests. A large number of dislocation line pile-ups can be clearly observed. The density of dislocation is closely related to the value of power dissipation efficiency η at some levels. When the value of η is about 0.36, the dislocation density is relatively small, and dislocation lines present a certain direction. When the value of η is less than 0.30, the degree of dislocation motion increases, and local dislocation pile-up is clearly observed. As the

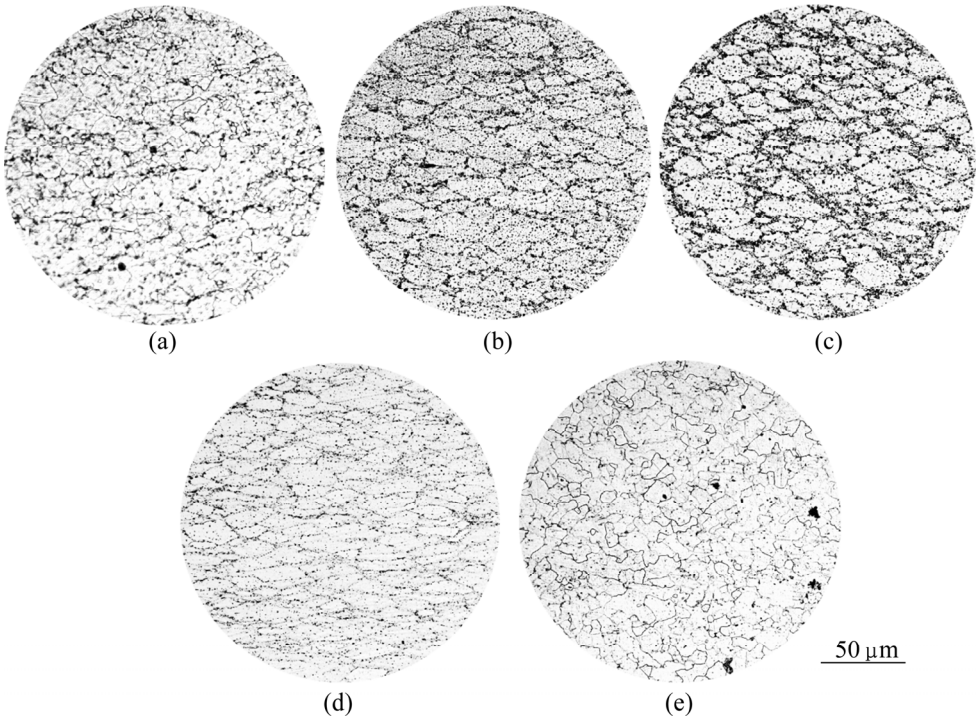

Fig. 9 Microstructures of hot-deformed spray forming LSHR alloy under different conditions: (a) 1110 °C, 0.01 s^{-1}; (b) 1050 °C, 0.001 s^{-1}; (c) 1020 °C, 0.0003 s^{-1}; (d) 1050 °C, 0.1 s^{-1}; (e) 1150 °C, 0.01 s^{-1}

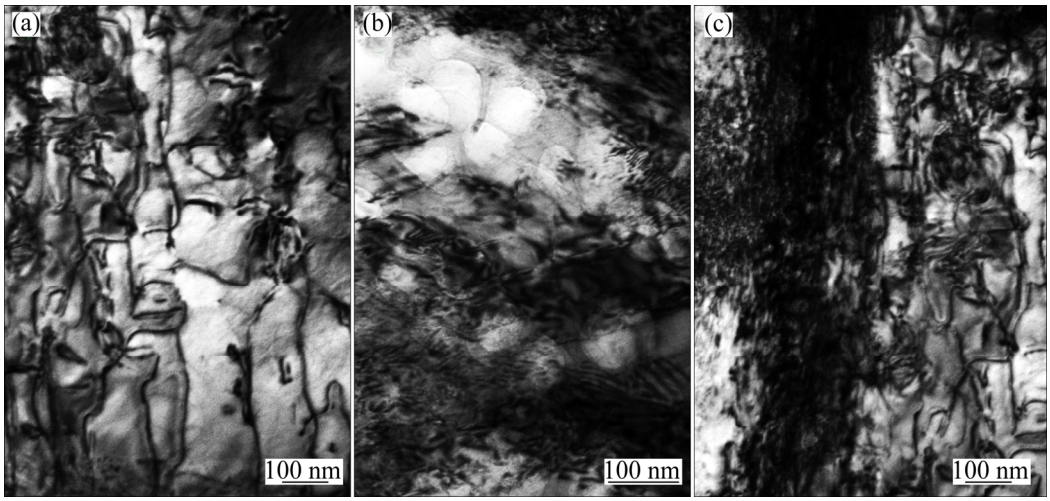

Fig. 10 Dislocation distribution of deformed samples at strain of 0.5 and different values of η: (a) η=0.36, 1150 °C, 0.01 s^{-1}; (b) η<0.30, 1020 °C, 0.1 s^{-1}; (c) η<0.24, 1050 °C, 1 s^{-1}

value of η is less 0.24, the dislocation density increases continuously, which indicates that dislocation motion is aggravated during the hot deformation. Hence, the trend of microstructure evolution corresponds to the domains on the power dissipation maps with different values of η to some extent, which further proves that the established power dissipation map is reliable.

3.4 Processing map

The optimum hot working process parameters cannot be completely confirmed based on the values of η in the power dissipation map because the materials may be in the stability or flow instability domains during the hot compression test. In other words, the high η value does not mean that the material has an excellent hot working performance. Therefore, it is very important to estimate the process instability domains of alloy under the flow stress. A continuum criterion for the occurrence of flow instability is obtained by utilizing the principle of the maximum rate of entropy production and expressed by

$$\xi(\dot{\varepsilon}) = \frac{\partial \ln\left(\frac{r}{r+1}\right)}{\partial \ln \dot{\varepsilon}} + r \tag{19}$$

where $\xi(\dot{\varepsilon})$ is the instability parameter. The flow instability is considered to occur when $\xi(\dot{\varepsilon})$ <0. The processing map is obtained through superimposing an instability map on a power dissipation map as shown in Fig. 11. These maps reveal the limiting temperature, strain rate and strain conditions under which fractures and instability occur during the deformation. The instability domains always locate in the region of high strain rates under different strains, indicating that the spray forming LSHR alloy is highly sensitive to the strain rate. With high η values, the domains marked as *S* at strains of 0.1, 0.3, 0.5 and 0.7, respectively remain in the processing maps. With increasing strain, domains marked as *S* are covered in larger shadow area (the shaded region corresponds to instability domain). When the strain increases to 0.7, the instability domains almost cover the whole area of processing map at low temperatures and high strain rates, indicating that the stability domain decreases with increasing strain level. Hence, it is recommended that the isothermal forging strain of the spray forming LSHR alloy should be not higher than 0.7 in order to ensure hot working process stability.

Table 2 shows the values of temperature and strain rate in the stability and instability domains with a higher η value at different strains in detail. These results provide a theoretical reference for the actual hot working process optimization of the spray forming LSHR alloy. Within the range of deformation conditions used in this work, the optimum processing parameters for the spray forming LSHR alloy are as follows: When the strain is 0.1, the optimum processing parameter is in a temperature range of 1110−1150 °C and a strain rate range of 0.006−0.2 s^{-1} with the η value of 0.38. When the strain is 0.3, the optimum processing parameter is in a temperature range of 1125−1150 °C and a strain rate range of 0.01−0.2 s^{-1} with the η value of 0.39. When the strain is 0.5, the optimum processing parameter is in a temperature range of 1110−1150 °C and a strain rate range of 0.01−0.3 s^{-1} with the η value of 0.36. When the strain is 0.7, the optimum processing parameter is in a temperature range of 1095−1145 °C and a strain rate range of 0.02−0.1 s^{-1} with the η value of 0.36. These results indicate that the optimum processing condition for good workability of the spray forming LSHR alloy depends on higher deformation temperature and lower strain rate during the hot deformation.

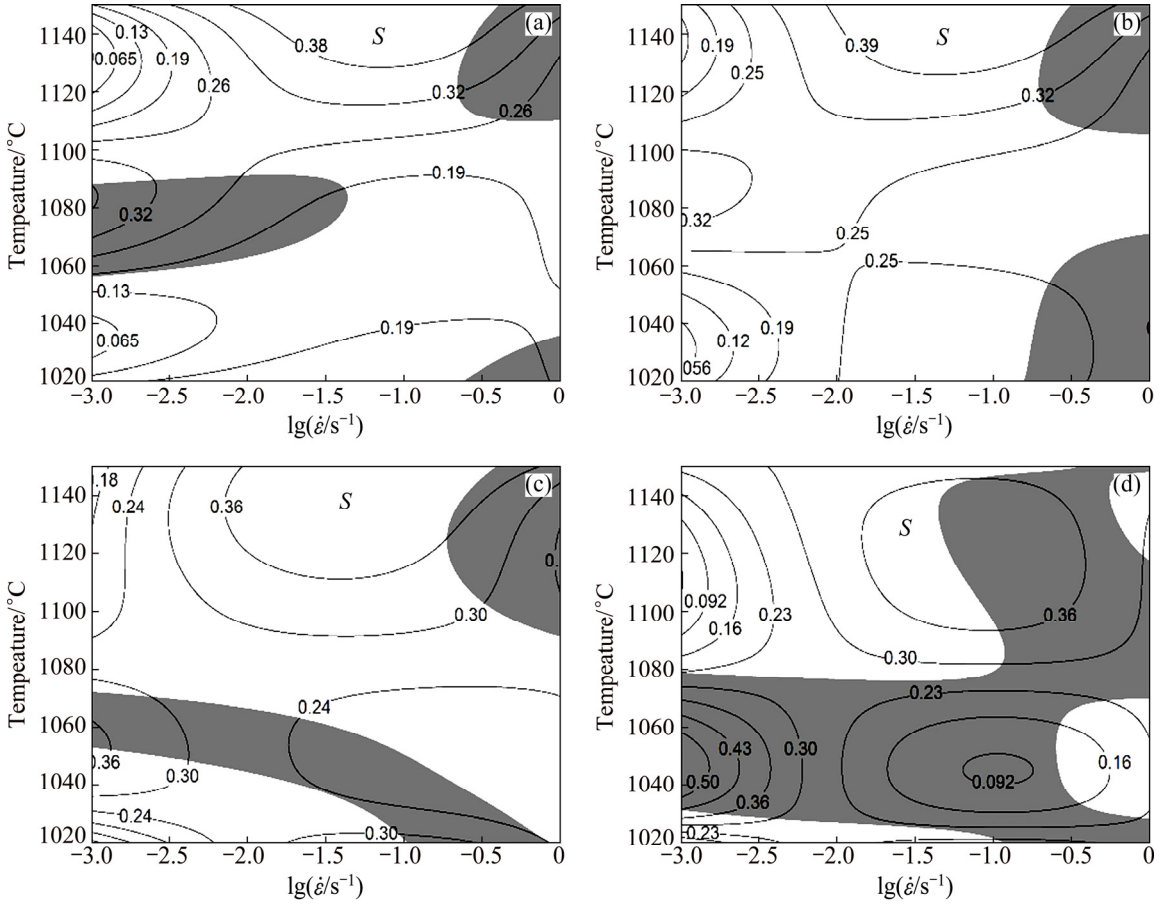

Fig. 11 Processing maps for spray forming LSHR alloy at different strains: (a) ε=0.1; (b) ε=0.3; (c) ε=0.5; (d) ε=0.7

Table 2 Stability and instability domains with high η values at different strains

Strain	η value	Stability domain	Instability domain
0.1	0.38	1110−1150 °C, 0.006−0.2 s^{-1} (Zone *S*)	1130−1150 °C, 0.2−0.5 s^{-1}
	0.32	1088−1097 °C, 0.001−0.003 s^{-1}; 1115−1150 °C, 0.003−0.3 s^{-1}	1070−1088 °C, 0.001−0.002 s^{-1}; 1120−1150 °C, 0.2−1 s^{-1}
0.3	0.39	1125−1150 °C, 0.01−0.2 s^{-1} (Zone *S*)	1130−1150 °C, 0.2−0.6 s^{-1}
	0.32	1075−1100 °C, 0.001−0.003 s^{-1}; 1110−1150 °C, 0.004−0.2 s^{-1}	1120−1150 °C, 0.2−1 s^{-1}
0.5	0.36	1110−1150 °C, 0.01−0.3 s^{-1} (Zone *S*)	1120−1150 °C, 0.2−0.6 s^{-1}; 1050−1060 °C, 0.001−0.002 s^{-1}
	0.30	1070−1075 °C, 0.001−0.003 s^{-1}; 1036−1053 °C, 0.001−0.005 s^{-1}; 1090−1150 °C, 0.003−0.3 s^{-1}	1050−1075 °C, 0.001−0.005 s^{-1}; 1100−1150 °C, 0.2−1 s^{-1}
0.7	0.50		1035−1057 °C, 0.001−0.002 s^{-1}
	0.43		1030−1065 °C, 0.001−0.003 s^{-1}
	0.36	1095−1145 °C, 0.02−0.1 s^{-1} (Zone *S*)	1030−1070 °C, 0.001−0.004 s^{-1}; 1095−1145 °C, 0.05−0.4 s^{-1}

4 Conclusions

1) The true stress−true strain flow curves of the spray forming LSHR alloy show the typical characteristics of dynamic recrystallization and dynamic recovery. The flow stress increases with decreasing deformation temperature and increasing strain rate. A hot deformation constitutive equation is given to characterize the dependence of flow stress on the temperature and strain rate. According to the hot compression tests, the activation energy of Q=1243.86 kJ/mol is determined.

2) The values of power dissipation efficiency (η) in the power dissipation maps are well correlated with DRX microstructure evolution and dislocation distribution. With increasing η value, the deformation microstructure exhibits finer and more homogeneous equiaxed DRX grains and lower dislocation density.

3) Based on comprehensive analysis of processing maps and microstructure observations, within the range of deformation conditions used in this work, the optimum processing parameters for the spray forming LSHR alloy at different strains are obtained. When the strain is 0.1, the optimum processing parameters are temperatures of 1110−1150 °C and strain rates of 0.006−0.2 s^{-1}. When the strain is 0.3, the optimum processing parameters are temperatures of 1125−1150 °C and strain rates of 0.01−0.2 s^{-1}. When the strain is 0.5, the optimum processing parameters are temperatures of 1110−1150 °C and strain rates of 0.01−0.3 s^{-1}. When the strain is 0.7, the optimum processing parameters are temperatures of 1095−1145 °C and strain rates of 0.02−0.1 s^{-1}. Therefore, the isothermal forging strain of the spray forming LSHR alloy should be not higher than 0.7.

References

[1] HUDA Z, EDI P. Materials selection in design of structures and engines of supersonic aircrafts: A review [J]. Materials and Design, 2013, 46: 552−560.

[2] OSADA T, GU Y F, NAGASHIMA N, YUAN Y, YOKOKAWA T, HARADA H. Optimum microstructure combination for maximizing tensile strength in a polycrystalline superalloy with a two-phase structure [J]. Acta Materialia, 2013, 61: 1820−1829.

[3] OLA O T, DOERN F E. A study of cold metal transfer clads in nickel-base INCONEL 718 superalloy [J]. Materials and Design, 2014, 57: 51−59.

[4] SENKOV O N, MAHAFFEY D W, SEMIATIN S L, WOODWARD C. Site-dependent tension properties of inertia friction-welded joints made from dissimilar Ni-based superalloys [J]. Journal of Materials Engineering and Performance, 2015, 24: 1173−1184.

[5] SEMIATIN S L, MCCLARY K E, ROLLETT A D, ROBERTS C G, PAYTON E J, ZHANG F, GABB T P. Microstructure evolution during supersolvus heat treatment of a powder metallurgy nickel-base superalloy [J]. Metallurgical and Materials Transactions A, 2012, 43: 1649−1661.

[6] SEMIATIN S L, KIM S L, ZHANG F, TILEY J S. An investigation of high-temperature precipitation in powder-metallurgy, gamma/gamma-prime nickel-base superalloys [J]. Metallurgical and Materials Transactions A, 2015, 46: 1715−1730.

[7] SEMIATIN S L, MCCLARY K E, ROLLETT A D, ROBERTS C G, PAYTON E J, ZHANG F, GABB T P. Plastic flow and microstructure evolution during thermomechanical processing of a PM nickel-base superalloy [J]. Metallurgical and Materials Transactions A, 2013, 44: 2778−2298.

[8] GRANT P S. Solidification in spray forming [J]. Metallurgical and Materials Transactions A, 2007, 38: 1520−1529.

[9] MIRZADEH H, ROOSTAEI M, PARSA M H, MAHMUDI R. Rate controlling mechanisms during hot deformation of Mg−3Gd−1Zn magnesium alloy: Dislocation glide and climb, dynamic recrystallization, and mechanical twinning [J]. Materials and Design, 2015, 68: 228−231.

[10] HAN Ying, WU Hua, ZHANG Wei, ZOU De-ning, LIU Gui-wu, QIAO Guan-jun. Constitutive equation and dynamic recrystallization behavior of as-cast 254SMO super-austenitic stainless steel [J]. Materials and Design, 2015, 69: 230−240.

[11] LIU Yan-hui, YAO Ze-kun, NING Yong-quan, NAN Yang, GUO Hong-zhen, QIN Chun, SHI Zhi-feng. The flow behavior and constitutive equation in isothermal compression of FGH4096-GH4133B dual alloy [J]. Materials and Design, 2014, 63: 829−837.

[12] CHAMANFAR A, JAHAZI M, GHOLIPOUR J, WANJARA P, YUE S. Evolution of flow stress and microstructure during isothermal compression of Waspaloy [J]. Materials Science and Engineering A, 2014, 615: 497−510.

[13] CHAMANFAR A, JAHAZI M, GHOLIPOUR J, WANJARA P, YUE S. Modeling grain size and strain rate in linear friction welded waspaloy [J]. Metallurgical and Materials Transactions A, 2013, 44: 4230−4238.

[14] YANG Yong-biao, ZHANG Zhi-min, LI Xu-bin, WANG Qiang, ZHANG Yan-hui. The effects of grain size on the hot deformation and processing map for 7075 aluminum alloy [J]. Materials and Design, 2013, 51: 592−597.

[15] MA Wen-bin, LIU Guo-quan, HU Ben-fu, ZHANG Yi-wen, LIU Jian-tao. Effect of Hf on carbides of FGH4096 superalloy produced by hot isostatic pressing [J]. Materials Science and Engineering A, 2013, 587: 313−319.

[16] LIAO Shu-lun, ZHANG Li-wen, YUE Chong-xiang, PEI Ji-bin, GAO Hui-ju. Hot deformation behaviors and flow stress model of GCr15 bearing steel [J]. Journal of Central South University of Technology, 2008, 15: 575−580.

[17] MOHAMMADI SHORE F, MORAKABATI M, ABBASI S M, MOMENI A, MAHDAVI R. Hot ductility of Incoloy 901 produced by vacuum arc remelting [J]. ISIJ International, 2014, 54: 1353−1360.

[18] DETROIS M, HELMINK R C, TIN S. Hot deformation characteristics of a polycrystalline gamma-gamma'-delta ternary eutectic Ni-base superalloy [J]. Materials Science and Engineering A, 2013, 586: 236−244.

[19] YEOM J T, KIM J H, HONG J K, KIM S W, PARK C H, NAM T H. Hot forging design of as-cast NiTi shape memory alloy [J]. Materials Research Bulletin, 2014, 58: 234−238.

[20] WEN D X, LIN Y C, LI H B, CHEN X M, JIAO D, LI L T. Hot deformation behavior and processing map of a typical Ni-based superalloy [J]. Materials Science and Engineering A, 2014, 591: 183−192.

[21] LIU Yan-hui, NING Yong-quan, YAO Ze-kun, GUO Hong-zhen, NAN Yang. Effect of true strains on processing map for isothermal compression of Ni−20.0Cr−2.5Ti−1.5Nb−1.0Al Ni-base superalloy [J]. Journal of Alloys and Compounds, 2014, 612: 56−63.

[22] WANG Ying, PAN Qing-lin, SONG Yan-fang, LI Chen, LI Zhi-feng. Hot deformation and processing maps of X-750 nickel-based superalloy [J]. Materials and Design, 2013, 51: 154−160.

[23] AMIRI A, SADEGHI M H, EBRAHIMI G R. Characterization of hot deformation behavior of AMS 5708 nickel-based superalloy using processing map [J]. Journal of Materials Engineering and Performance, 2013, 22: 3940−3945.

[24] PU En-xiang, ZHENG Wen-jie, XIANG Jin-zhong, SONG Zhi-gang, LI Ji. Hot deformation characteristic and processing map of superaustenitic stainless steel S32654 [J]. Materials Science and Engineering A, 2014, 598: 174−182.

[25] SENTHILKUMAR V, BALAJI A, NARAYANASAMY R. Analysis of hot deformation behavior of Al 5083-TiC nanocomposite using constitutive and dynamic material models [J]. Materials and Design, 2012, 37: 102−110.

[26] RAJAMUTHAMILSELVAN M, RAMANATHAN S. Development of processing map for 7075 Al/20% SiC_p composite [J]. Journal of Materials Engineering and Performance, 2012, 21: 191−196.

[27] YANG Zhi-nan, ZHANG Fu-cheng, ZHENG Chun-lei, ZHANG Ming, LÜ Bo, QU Lin. Study on hot deformation behaviour and processing maps of low carbon bainitic steel [J]. Materials and Design, 2015, 66: 258−266.

[28] NING Y Q, FU M W, YAO W. Recrystallization of the hot isostatic pressed nickel-base superalloy FGH4096: I. Microstructure and mechanism [J]. Materials Science and Engineering A, 2011, 528: 8065−8070.

[29] RAJ R. Development of a processing map for use in warm-forming and hot-forming processes [J]. Metallurgical Transactions A, 1981, 12: 1089−1097.

基于本构方程和热加工图的喷射成形 LSHR 合金的热变形行为

徐 轶，汪 杰

西南交通大学 材料科学与工程学院，成都 610031

摘 要：采用 Gleeble−3500 热模拟试验机在温度为 1020~1150 °C、应变速率为 0.0003~1.0 s^{-1} 条件下，对喷射成形低固溶高熔点(LSHR)合金进行热压缩实验，研究其流变行为。建立其本构方程，绘制能量耗散图以及热加工图，观察基于不同能量耗散因子的微观演变和位错分布特征。结果表明，流变应力随温度的降低、应变速率增加而增大。经计算，喷射成形 LSHR 合金的变形激活能为 1243.83 kJ/mol。当应变为 0.5 时，在加工图能量耗散因子 η=0.36 区域中微观组织呈典型的动态再结晶和低位错密度特征。基于微观组织演变和热加工图，喷射成形 LSHR 合金的最佳热加工参数范围为热加工温度 1110~1150 °C、应变速率 0.01~ 0.3 s^{-1}。

关键词：低固溶高熔点(LSHR)合金；流变行为；热加工性；能量耗散图；加工图；动态再结晶

(Edited by Wei-ping CHEN)